Research Article | Vol. 33, No. 19 / 22 Sep 2025 / Optics Express 40465
Optics EXPRESS

Evaluation of near-blue UV remote sensing reflectance over the global ocean from SNPP VIIRS, PACE OCI, and GCOM-C SGLI

LUFEI ZHENG,[1] ZHONGPING LEE,[1,*] YONGCHAO WANG,[2] XIAOLONG YU,[1] WENDIAN LAI,[1] AND SHAOLING SHANG[1]

[1]State Key Laboratory of Marine Environmental Science, College of Ocean and Earth Sciences, Xiamen University, Xiamen 361102, China
[2]Tianjin Research Institute for Water Transport Engineering, National Engineering Research Center of Port Hydraulic Construction Technology, Tianjin 300456, China
[*]zhongping.lee@umb.edu

Abstract: Solar radiation in the ultraviolet (UV) bands plays an important role in marine biogeochemical processes, and at the same time, measurements of a satellite sensor in the UV help the data processing of ocean color satellites. However, historically, satellite ocean color missions lack UV measurements; only in recent years have there been satellite sensors, such as PACE OCI, to provide a direct measurement of radiance in the near-blue UV (nbUV) domain. To address the limitation of earlier measurements, a deep-learning-based system (termed $UVISR_{dl}$) has been previously introduced to estimate remote-sensing reflectance (R_{rs}) of the nbUV bands at 360, 380, and 400 nm from R_{rs}(visible). In this study, as PACE OCI offers global-ocean hyperspectral R_{rs} products from UV to visible bands, we leveraged this opportunity to comprehensively evaluate the performance of this $UVISR_{dl}$ system and compare the R_{rs}(nbUV) among VIIRS, OCI, and SGLI. It is found that the R_{rs}(nbUV) values from VIIRS and OCI exhibit high consistency, with mean absolute unbiased relative difference (MAURD) ranging from ~0.23–0.30 at 360 nm, ~0.21–0.22 at 380 nm, and ~0.17–0.20 at 400 nm, while the SGLI shows lower consistency compared to the former two (MAURD = ~0.47 at 380 nm). More importantly, the consistency assessment metrics in R_{rs}(nbUV) between VIIRS and OCI are nearly the same, regardless of whether the OCI R_{rs}(nbUV) were derived from $UVISR_{dl}$ or measured directly. These findings demonstrate $UVISR_{dl}$'s potential for extending global-scale UV reflectance back into periods lacking direct UV observations, enabling the generation of long-term remote-sensing products, and deepening our understanding of the interactions between UV radiation and biogeochemical processes in the global ocean.

1. Introduction

Ultraviolet (UV) radiation plays a crucial role in the biological system on Earth. The UV radiation reaching Earth's surface covers approximately 280–400 nm, as wavelengths shorter than ~280 nm are almost entirely absorbed in the upper stratosphere [1,2]. In the ocean, UV radiation not only affects the photosynthesis of phytoplankton [3] but also contributes to the photolysis of dissolved organic matter (DOM) [4,5]. Many aquatic species employ adaptive strategies to mitigate effects of UV radiation, including vertical migration and synthesis of UV-absorbing substances [6,7]. Among these protective mechanisms, mycosporine-like amino acids (MAAs) are widely synthesized or accumulated by diverse marine and freshwater organisms for UV protection [8]. Moreover, the photolytic degradation of DOM by UV radiation produces lower molecular weight compounds, altering their bioavailability for bacterioplankton uptake [5]. Further, UV radiation affects carbon and nitrogen cycling in both terrestrial and aquatic ecosystems [7,9]. Therefore, measuring UV radiation across broad spatial and temporal scales is

#568441 https://doi.org/10.1364/OE.568441
Journal © 2025 Received 21 May 2025; revised 23 Aug 2025; accepted 3 Sep 2025; published 16 Sep 2025

Optics EXPRESS

essential for comprehensively understanding light-ocean interaction processes and their role in biogeochemical cycling and climate change.

Ocean color remote sensing provides an effective and practical approach for acquiring large-scale, long-term observations of UV radiation in marine environments. In practice, satellite measurements in the UV are technically constrained, particularly below 350 nm, due to the reduced sensitivity of optical instruments, low solar irradiance, and stronger atmospheric contribution due to Rayleigh scattering [10]. As a result, the 350–400 nm range (near-blue UV, nbUV hereafter) is the most feasible portion of the UV spectrum for ocean color remote sensing.

Despite this narrow spectral window, it remains important in many aspects. Knowing radiance information in the nbUV has been shown to be helpful for satellite ocean color retrievals. For instance, many analyses have confirmed that extending measurements into the nbUV enables more accurate atmospheric correction under absorbing aerosol conditions [11–13], and also improves the correction performance in turbid coastal waters [14]. Moreover, access to nbUV in ocean color measurements would also improve the retrieval of the absorption coefficients of colored dissolved organic matter (CDOM) ($a_g(\lambda)$; m^{-1}) [12,15–17] and phytoplankton ($a_{ph}(\lambda)$; m^{-1}) [18]. All these suggest the necessity of obtaining nbUV observations from satellites.

Over the past decades, ocean color satellite sensors such as the Sea-viewing Wide Field-of-view Sensor (SeaWiFS), MODerate resolution Imaging Spectroradiometer (MODIS), Visible Infrared Imaging Radiometer Suite (VIIRS) have focused on visible-NIR bands (typically > 410 nm for ocean color measurements), leaving a gap in our ability to monitor UV radiation in the global ocean. To date, only a few recent ocean color satellites have started to include measurements in the nbUV domain. For example, the Ocean and Land Colour Instrument (OLCI) on Sentinel 3 (launched in 2016, has a 400 nm band) [19], the Second Generation Global Imager (SGLI) on the Global Change Observation Mission (GCOM-C, launched in 2017, 380 nm) [20], the Ultraviolet Imager (UVI) on HaiYang-1C (HY-1C, launched in 2018, 355 and 385 nm) [21], and the Ocean Color Instrument (OCI) on the Plankton, Aerosol, Cloud, and ocean Ecosystem (PACE, 2024, ~350 nm and longer) [22–24], provide new opportunities to advance our understanding of UV penetration in the marine environment. However, the duration of these observations remains relatively limited.

To address this data gap, Wang et al. [25] and Liu et al. [26] developed deep-learning-based systems to estimate remote-sensing reflectance (R_{rs}) in the nbUV (termed as R_{rs}(nbUV)) from R_{rs} data in the visible bands (termed as R_{rs}(visible)), laying the groundwork to generate decade-long R_{rs}(nbUV). Wang et al. [25] introduced a straightforward end-to-end neural framework (termed $UVISR_{dl}$ system) using the R_{rs}(visible) at 410, 440, 490, 550, and 670 nm as input, whereas Liu et al. [26] proposed an algorithm-switching approach using more comprehensive input features. The previous analysis regarding the $UVISR_{dl}$ system provided in Wang et al. [25] indicated excellent performance, but that was limited to the data collected from field measurements; the global applicability of the model remains unknown. The hyperspectral R_{rs} data provided by the PACE satellite, extending from UV to near-infrared at 2.5 nm or 1.25 nm intervals, provide a great opportunity to evaluate the deep-learning system using data from the global ocean and to examine the system's utility and limitations across diverse marine environments. In addition, it is possible to compare the nbUV data from OCI with those from VIIRS and from SGLI (which includes a UV band and has a band configuration similar to VIIRS), thus potentially extending R_{rs}(nbUV) products to earlier days with confidence.

The structure of this paper is as follows: Section 2 provides an overview of the data and processing methods used for the evaluation. Section 3 introduces the deep-learning scheme $UVISR_{dl}$ and evaluates its performance using data from PACE OCI. Section 4 examines the consistency of R_{rs}(nbUV) among Suomi National Polar-orbiting Partnership (SNPP) VIIRS (SNPP VIIRS), PACE OCI, and GCOM-C SGLI, while Section 5 offers an in-depth discussion of

Optics EXPRESS

the findings. Finally, Section 6 summarizes the main conclusions and outlines potential directions for future research.

2. Data and methods

2.1. Satellite data processing

Satellite data from the three ocean color sensors, SNPP VIIRS, PACE OCI, and GCOM-C SGLI (hereinafter referred to as VIIRS, OCI, and SGLI, respectively), were utilized in this study. Level-2 satellite data within ±3 hours of *in situ* measurements taken at MOBY (Marine Optical BuoY) [27] and AERONET-OC (AErosol RObotic NETwork-Ocean Color) [28], from May to December 2024, were obtained to evaluate the consistency between satellite-derived and field-measured values. In addition, Level-3 monthly composite data from May to December were analyzed to compare the consistency among different satellite products across the global ocean, with that of September 2024 selected as a representative example. The use of Level-3 monthly composites helps reduce uncertainties associated with data processing and reduces data gaps inherent in daily or instantaneous observations, thereby enhancing the comparability and robustness of multi-satellite products. September was chosen as an illustrative example because the quality of global R_{rs} data of this month is less affected by sea ice in the polar regions, avoiding potential biases due to unmasked data points associated with sea ice, although results from other months were generally similar.

For this study, the latest version of VIIRS and OCI (Version 3.0) data were acquired from the Ocean Color Web supported by the Ocean Biology Processing Group (OBPG) at NASA's Goddard Space Flight Center (https://oceancolor.gsfc.nasa.gov/), and SGLI Level-2 and Level-3 monthly composite data were obtained from the Japan Aerospace Exploration Agency (JAXA) G-Portal web site (Global Portal, https://gportal.jaxa.jp/gpr/) and JAXA Satellite Monitoring for Environmental Studies (JASMES, https://www.eorc.jaxa.jp/JASMES/), respectively. It is worth noting that the three satellite sensors differ in spectral configurations. VIIRS and SGLI are multispectral sensors with relatively similar band settings in the visible and near-infrared range. VIIRS features five moderate-resolution bands in the visible range, centered at 410, 443, 486, 551, and 671 nm, with bandwidths ranging between 15 and 39 nm [29,30]. SGLI offers eight spectral bands for ocean color observation, centered at 380, 412, 443, 490, 530, 565, 670, and 865 nm, with bandwidths ranging between 10 and 20 nm [31]. In contrast, OCI is a hyperspectral sensor that provides continuous 2.5 nm intervals from approximately 346 to 719 nm and an enhanced 1.25 nm interval between 640 and 715 nm [32].

2.2. MOBY

MOBY has been operated off Lanai Island in Hawaii (around 20.82° N, 157.19° W in the 271st deployment) since July 1997 [27]. It is currently a National Oceanic and Atmospheric Administration (NOAA) funded project to provide data for vicarious calibration of ocean color satellites. The satellite band-weighted MOBY-Refresh data, which are consistent with the satellite bands, have been available since May 1, 2024, from the NOAA CoastWatch homepage (https://coastwatch.noaa.gov/cwn/products/ocean-color-radiances-moby-field-observations.html), and they were used in this study.

2.3. AERONET-OC

AERONET-OC provides above-water radiometric data gathered with sun photometers installed on offshore platforms like lighthouses, oceanography, and oil towers. The uncertainty is at the 4–5% level for the water-leaving radiance data in the blue-green spectral regions obtained by AERONET-OC [33]. The Level 1.5 data from the available AERONET-OC sites (AAOT, ARIAKE_TOWER_2, Bahia_Blanca, Casablanca_Platform, Chesapeake_Bay, Frying_Pan_Tower,

Optics EXPRESS

Gustav_Dalen_Tower, Irbe_Lighthouse, Kemigawa_Offshore, Lake_Erie, LISCO, Lucinda, MVCO, Palgrunden, PLOCAN_Tower, San_Marco_Platform, Section-7_Platform, Socheongcho, USC_SEAPRISM, and WaveCIS_Site_CSI_6) operated from May to December 2024 were obtained from the AERONET official website (https://aeronet.gsfc.nasa.gov/) to evaluate the R_{rs} Level-2 products from satellites. The obtained AERONET-OC data generally consists of 20 bands centered at 400, 412, 440, 443, 490, 500, 510, 532, 551, 555, 560, 620, 667, 675, 681, 709, 779, 865, 870, and 1020 nm; however, not all sites have consistent bands. In this study, the band-conversion method of Mélin and Sclep [34] was applied to convert AERONET-OC data to the band configurations of VIIRS and SGLI, while the method of Talone et al. [35] was used to convert the AERONET-OC data to OCI bands, following the band-conversion principles used in the ThoMaS match-up toolkit (endorsed by NASA tutorials: https://oceancolor.gsfc.nasa.gov/resources/docs/tutorials/).

2.4. Data matching method

The matchup criteria and procedures outlined by Bailey and Werdell [36] were employed to obtain matchups between satellite Level-2 and *in situ* data. A time window of ±3 hours was applied to pair the *in situ* and satellite observations. A 3×3 pixel window centered at the *in situ* location was used to extract and aggregate satellite-derived R_{rs}, retaining only pixels exempt from the following flags: land, cloud, ice, straylight, high/moderate glint, very low/negative water-leaving radiance, or atmospheric correction failure [36]. The dataset used for these matchups spans from May to December 2024 and follows the above-described matching method to ensure that the satellite and *in situ* data are temporally aligned and valid for this study. For comparison among satellite Level-3 products, the VIIRS and OCI Level-3 data, having identical spatial resolutions of 4 km, were directly matched on a pixel-by-pixel basis. SGLI Level-3 data, originally at a spatial resolution of 5 km, were resampled to 4 km before performing pixel-level matching with VIIRS and OCI, ensuring spatial alignment and consistency across datasets.

2.5. Accuracy assessment metrics

To evaluate the consistency between any two datasets, we calculated several commonly used statistical metrics, including the coefficient of determination (R^2) in linear regression analysis, root mean square difference (RMSD; unit: sr^{-1}, Eq. (1)), bias (unit: sr^{-1}, Eq. (2)), and the mean absolute unbiased relative difference (MAURD, Eq. (3)). R^2 evaluates the strength of the linear relationship between two datasets; RMSD represents the overall magnitude of their differences; bias quantifies the average deviations; and MAURD expresses relative differences, which is particularly suitable for assessing the consistency between two datasets in cases where neither can serve as "truth" [25]. The math expressions for RMSD, bias, and MAURD are as below,

$$\mathrm{RMSD} = \sqrt{\frac{1}{N}\sum_{i=1}^{N}(Data_{1,i} - Data_{2,i})^2}, \tag{1}$$

$$\mathrm{bias} = \frac{1}{N}\sum_{i=1}^{N}(Data_{1,i} - Data_{2,i}), \tag{2}$$

$$\mathrm{MAURD} = \frac{1}{N}\sum_{i=1}^{N}\left|\frac{Data_{1,i} - Data_{2,i}}{Data_{1,i} + Data_{2,i}}\right| \times 2, \tag{3}$$

where $Data_{1,i}$ and $Data_{2,i}$ represent data at the i-th pixel from two independent determinations, corresponding to the X-axis and Y-axis data in a scatter plot, and N is the total number of samples.

Optics EXPRESS

In addition, at a pixel, the unbiased relative difference (URD) between two measurements is calculated as Eq. (4), which is used to examine the spatial distribution of consistency between two datasets for the same property,

$$\mathrm{URD}_i = \frac{Data_{1,i} - Data_{2,i}}{Data_{1,i} + Data_{2,i}} \times 2. \tag{4}$$

3. Deep-learning system for R_{rs}(nbUV): UVISR$_{dl}$

3.1. Brief description of the UVISR$_{dl}$ system

UVISR$_{dl}$ is a deep-learning model that estimates R_{rs}(nbUV) (specifically for 360, 380, and 400 nm) based on R_{rs}(visible), producing values that agree with field measurements within approximately 10% [25]. The model was developed based on 200,000 synthetic hyperspectral R_{rs} spectra, which were generated from 200,000 sets of inherent optical properties (IOPs) spanning a wide range of water types, covering wavelengths from 350 to 800 nm at 5 nm spectral resolution. The architecture includes 4 hidden layers with various neurons, designed to minimize prediction loss and achieve reliable results across different spectral bands. This model takes R_{rs}(visible) at 410, 440, 490, 550, and 670 nm as inputs that can be applied to both field and satellite R_{rs}, for which there are corresponding or analogous wavelength bands. Further details of UVISR$_{dl}$ can be found in Wang et al. [25].

3.2. Evaluation of UVISR$_{dl}$ with OCI measurements

We evaluated UVISR$_{dl}$ using OCI's global R_{rs} at visible bands and UV bands first. Specifically, we applied UVISR$_{dl}$ to obtain R_{rs} in the nbUV from OCI-measured R_{rs}(visible) and compared the results with OCI-measured R_{rs}(nbUV). Hereinafter, UVISR$_{dl}$-derived R_{rs} is appended with a subscript 'dl' (lowercase form of 'DL', representing deep learning) to the sensor name (e.g., OCI$_{dl}$), while the notation without such a subscript represents products directly from satellite measurements. It is worth noting that these data are completely independent of the data used to train UVISR$_{dl}$, providing a basis to assess the generalization capacity of UVISR$_{dl}$.

As shown in Figs. 1(a)–1(c), there is a remarkable consistency between OCI$_{dl}$ R_{rs}(nbUV) and OCI R_{rs}(nbUV) of global waters obtained from the monthly satellite composite OCI image of September 2024, particularly for both 380 and 400 nm, where near-perfect agreement is observed ($R^2 = 1.00$, RMSD = 0.0004 sr^{-1}, bias = -3.5 × 10^{-4} sr^{-1}, MAURD = 0.07). At 360 nm, although reasonably good agreement is still observed ($R^2 = 0.96$, RMSD = 0.0012 sr^{-1}, bias = 6.55 × 10^{-4} sr^{-1}, MAURD = 0.18), slightly larger deviations are noticed, likely due to a weaker relationship between the 360 nm band and visible bands. Furthermore, evaluation over the entire period from May to December 2024 confirms the stability of UVISR$_{dl}$ performance, with metrics at 360 nm ($R^2 = 0.94 \pm 0.01$, RMSD = 0.00126 ± 0.00012 sr^{-1}, bias = 4.5 × 10^{-4} ± 0.9 × 10^{-4} sr^{-1}, MAURD = 0.14 ± 0.02), at 380 nm ($R^2 = 0.98 \pm 0.002$, RMSD = 0.0007 ± 0.00005 sr^{-1}, bias = -1.6 × 10^{-4} ± 0.7 × 10^{-4} sr^{-1}, MAURD = 0.08 ± 0.01), and at 400 nm ($R^2 \approx 1.0$, RMSD = 0.0004 ± 0.00002 sr^{-1}, bias = -3.5 × 10^{-4} ± 0.1 × 10^{-4} sr^{-1}, MAURD = 0.07 ± 0.006).

Notably, as indicated by the red-circled points in Fig. 1(a), a group of data points exhibits a noticeable deviation from the overall trend. The data points in the red circle are largely distributed in high-latitude regions and were effectively separated by applying latitude thresholds at 50° N and 50° S, with the corresponding correlation plots shown in Figs. 1(d)–1(f). If this deviated group is excluded, the assessment metrics show a slight improvement, with R^2 increasing to 0.97 and MAURD dropping to 0.16 for 360 nm. For 380 and 400 nm, R^2 remains unchanged at 0.96 and 0.95, while MAURD decreases to 0.06 and 0.05, respectively. Figures 1(d)–1(f) show a clear wavelength-associated trend for waters in high-latitude regions, where the regression slope increases from 0.71 at 360 nm to 0.96 at 400 nm. This indicates a systematic bias at shorter

Optics EXPRESS

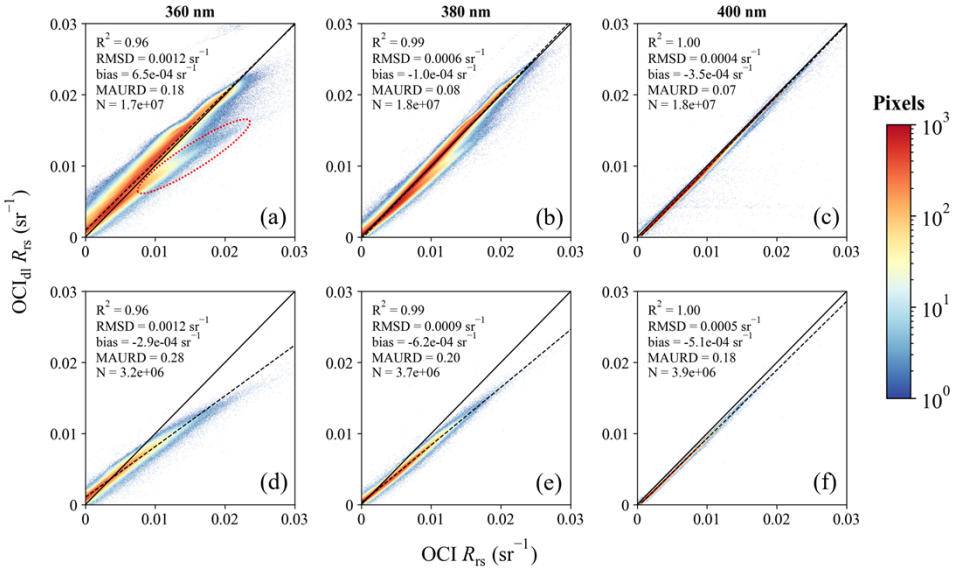

Fig. 1. Correlation plots between modeled OCI_{dl} R_{rs}(nbUV) and measured OCI R_{rs}(nbUV) obtained from the monthly satellite composite OCI image of September 2024, shown for (a–c) global waters, and (d–f) high-latitude waters (50°–90°S and 50°–90°N). In panel (a), the red-circled cluster of data points shows a noticeable deviation from the overall trend. The color scale "Pixels" indicates the point density, and the same applies to all similar figures.

wavelengths in high-latitude waters, likely caused by increased uncertainties in atmospheric correction under large solar zenith angles, where the effects of Earth's surface curvature become significant, as well as likely by stronger Rayleigh scattering and residual effects from clouds and surface reflection (e.g., whitecaps and sun glint) [37].

The above demonstrates that the R_{rs}(nbUV) could be well estimated from R_{rs}(visible) based on the $UVISR_{dl}$ system, at least for waters within 50° N and 50° S. This lays a strong foundation for generating global oceanic R_{rs}(nbUV) products for satellites having no UV capabilities but with robust R_{rs}(visible).

4. R_{rs}(nbUV) from VIIRS, OCI, and SGLI satellites

4.1. Comparison of VIIRS and OCI R_{rs} in the visible bands

Before applying the model to obtain comparable R_{rs}(nbUV) across different satellites, it is necessary to examine the consistency of the model inputs: the measured R_{rs}(visible) between VIIRS and OCI. We thus compared R_{rs} for both original and converted VIIRS R_{rs} data. Original VIIRS R_{rs} refers to the R_{rs} values of the actual bands at 410, 443, 486, 551, and 671 nm, whereas converted VIIRS R_{rs} are those of the bands shifted to 410, 440, 490, 550, and 670 nm. Following the approach of Wang et al. [25], this conversion is an empirical model based on deep learning developed using the same synthetic hyperspectral R_{rs} data as for the development of $UVISR_{dl}$, which converts a wideband R_{rs} product to a narrowband R_{rs}. Since OCI is a hyperspectral sensor (narrow band) and already provides the five bands required by the model, the original bands were directly used without the need for band conversion.

Figure 2 shows relationships between VIIRS R_{rs} (after band conversion) and OCI R_{rs} at the required bands for the $UVISR_{dl}$ model input (410, 440, 490, 550, and 670 nm), which were obtained from global monthly composite images of September 2024. In general, a high level of consistency is observed between VIIRS and OCI across most bands (Fig. 2). Specifically,

Optics EXPRESS

the MAURD values were 0.19, 0.17, 0.11, 0.13, and 0.27 at 410, 440, 490, 550, and 670 nm, respectively. In addition, all bands exhibited strong linear correlations between VIIRS and OCI, with R^2 values exceeding 0.8. Similar results were also found for VIIRS R_{rs} of the original blue-green bands. There is a substantial improvement for the 671 nm band though after the conversion, with a reduction of 22.7% in the MAURD value. This band is near the red peak of chlorophyll-a absorption; therefore, although the central wavelengths of VIIRS R_{rs}(671) and OCI R_{rs}(670) are nearly identical, differences in their spectral response functions (SRFs), particularly in bandwidth, likely caused the large R_{rs} difference before the conversion. These results indicate that band conversion can effectively minimize band-center and bandwidth-related discrepancies. This process is important, as it ensures that the R_{rs} values required for $UVISR_{dl}$ from both sensors are reasonably consistent and reliable for further applications and analyses.

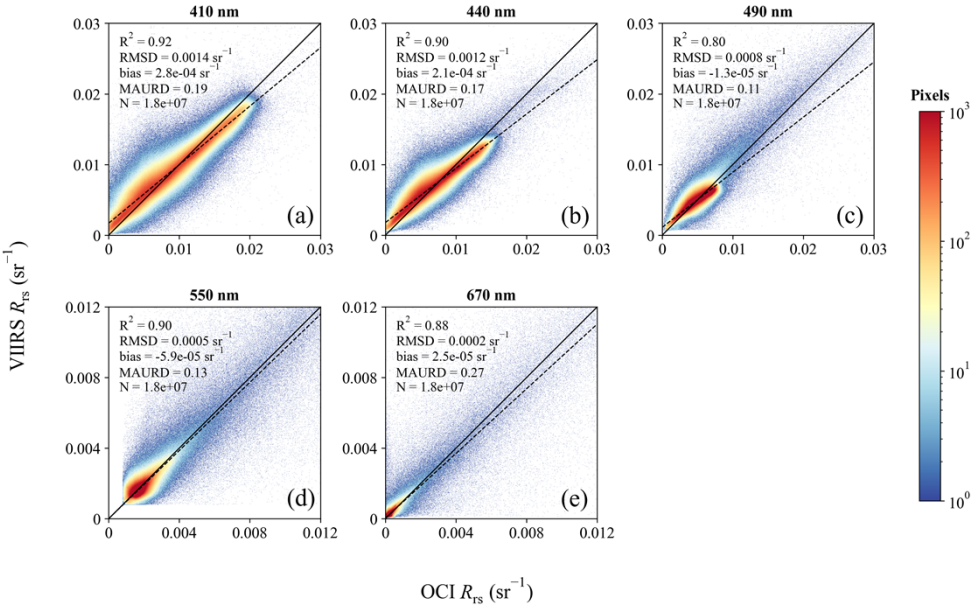

Fig. 2. Correlation plots between VIIRS R_{rs}(visible) and OCI R_{rs}(visible) for global waters obtained from monthly satellite composite images of September 2024. VIIRS data are converted to 410, 440, 490, 550, and 670 nm bands from the original bands using an empirical model, while OCI directly uses its original bands.

4.2. *VIIRS's R_{rs}(nbUV) vs OCI's R_{rs}(nbUV)*

Following the $UVISR_{dl}$ scheme developed by Wang et al. [25], R_{rs} at 360, 380, and 400 nm of VIIRS and OCI, respectively, were generated from the corresponding R_{rs} in the visible domain. Note that it is the same $UVISR_{dl}$ system applied to both VIIRS and OCI data for the generation of R_{rs}(nbUV), any differences between the $VIIRS_{dl}$ and OCI_{dl} R_{rs}(nbUV) are solely attributable to the systematic differences in R_{rs}(visible) between the two sensors, while the comparison between $VIIRS_{dl}$ and OCI R_{rs}(nbUV) further includes the discrepancies between the modeled and the measured results.

Figures 3(a)–3(c) first compares $VIIRS_{dl}$ R_{rs}(nbUV) with OCI R_{rs}(nbUV), showing strong correlations across 360–400 nm (R^2 = 0.8–0.92; MAURD = 0.17–0.30), with differences comparable to those in the visible bands (MAURD = 0.11–0.27, see Fig. 2). The correlations between OCI_{dl} and $VIIRS_{dl}$ R_{rs}(nbUV) across wavelengths from 360 to 400 nm are similar, with R^2 values ranging from 0.91–0.92 and MAURD ranging from 0.20 to 0.23 (Figs. 3(d)–3(f)). The MAURD

Optics EXPRESS

values in Figs. 3(a)–3(c) and Figs. 3(d)–3(f) decrease with increasing wavelengths, suggesting better agreement between $VIIRS_{dl}$ and OCI (or OCI_{dl}) R_{rs}(nbUV) at longer UV wavelengths. This result is consistent with the previous study, which compared VIIRS with MODIS [25], showing that consistency improves with increasing wavelength.

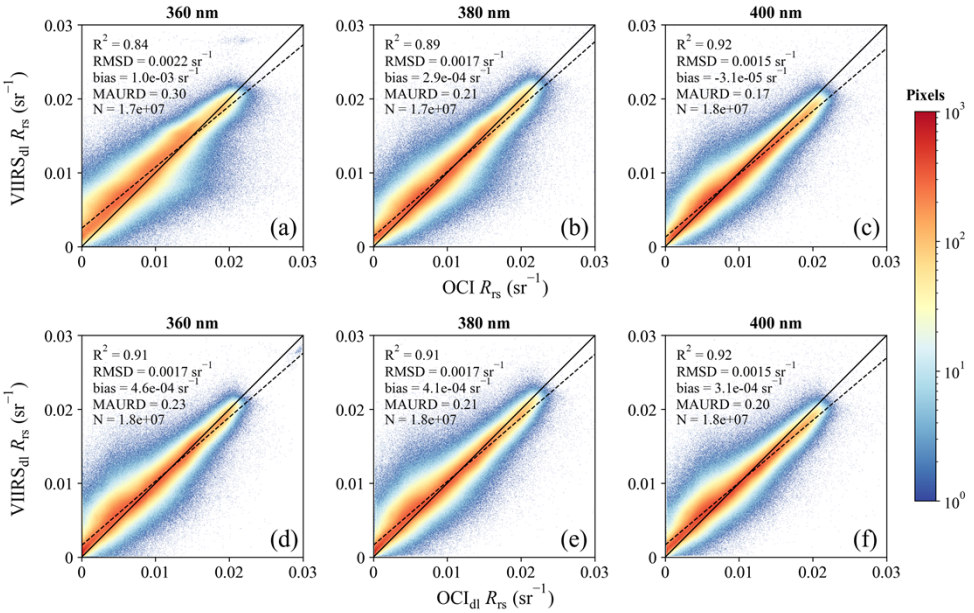

Fig. 3. Correlation plots between modeled $VIIRS_{dl}$ R_{rs}(nbUV) and measured OCI R_{rs}(nbUV) (upper panel: a–c) and between modeled $VIIRS_{dl}$ R_{rs}(nbUV) and modeled OCI_{dl} R_{rs}(nbUV) (lower panel: d–f) of global waters obtained from monthly satellite composite images of September 2024.

Note that the three comparison pairs, OCI_{dl} vs OCI, $VIIRS_{dl}$ vs OCI_{dl}, and $VIIRS_{dl}$ vs OCI, capture distinct error sources (systematic differences between model and observation, systematic differences in R_{rs}(visible) between the two sensors, and their combined effect). The comparison of MAURD for each pair reveals that visible-band differences between sensors introduce greater inconsistencies than model-observation differences alone (OCI_{dl} vs OCI). At 380 and 400 nm, the systematic bias results in a relatively low MAURD of only 0.07–0.08 between OCI_{dl} and OCI. However, the MAURD for $VIIRS_{dl}$ vs OCI more than doubled at these wavelengths, and it approaches ~0.30 at 360 nm. This level is non-negligible, highlighting a degree of inconsistency of the input R_{rs} between OCI and VIIRS, where differences propagate from the visible to the nbUV range during the $UVISR_{dl}$ process. Moreover, while $VIIRS_{dl}$ R_{rs}(360) exhibits notable discrepancies with OCI R_{rs}(360) (MAURD = 0.30), its agreement with OCI_{dl} R_{rs}(360) is better (MAURD = 0.23). The slightly higher discrepancies between $VIIRS_{dl}$ and OCI R_{rs}(360) indicate that while $VIIRS_{dl}$ can provide a reasonable estimate of R_{rs}(360) of the global ocean, it still has some residual bias compared to "true" R_{rs}(360), apart from the inter-satellite differences, especially the 360 nm band is relatively quite distant from the visible bands.

Building upon the findings shown in Fig. 3, which indicate that the discrepancies between $VIIRS_{dl}$ and OCI R_{rs}(nbUV) are slightly wavelength dependent, and particularly more pronounced at 360 nm, further investigation was prompted into the potential spatial patterns of these discrepancies. To this end, we compared the global distribution of URD between paired R_{rs}(nbUV) values from OCI, OCI_{dl}, and $VIIRS_{dl}$ for the monthly composite of September 2024. To avoid the redundant presentation of similar distribution patterns and to enable direct

Optics EXPRESS

comparison with the 380 nm band of SGLI, the URD of the 380 nm band (hereinafter referred to as URD(380)) was selected for illustration.

Figure 4 presents the global distribution of URD(380) for OCI_{dl} vs OCI, $VIIRS_{dl}$ vs OCI, and $VIIRS_{dl}$ vs OCI_{dl}, respectively (Figs. 4(a)–4(c)), with corresponding histograms of URD(380) depicted in Figs. 4(d)–4(f). Strong consistency is observed in R_{rs}(nbUV) between the OCI_{dl} and OCI, as indicated by the URD(380) values approaching zero (mean value = –0.01 and standard deviation = 0.18), with the exception of certain coastal regions at mid to high latitudes. Similarly, but with notable differences, the comparison between $VIIRS_{dl}$ and OCI (or OCI_{dl}) reveals a tendency for URD(380) to approach zero within equatorial to mid-latitude regions, yet exhibits higher URD(380) values at high latitudes and in various coastal areas.

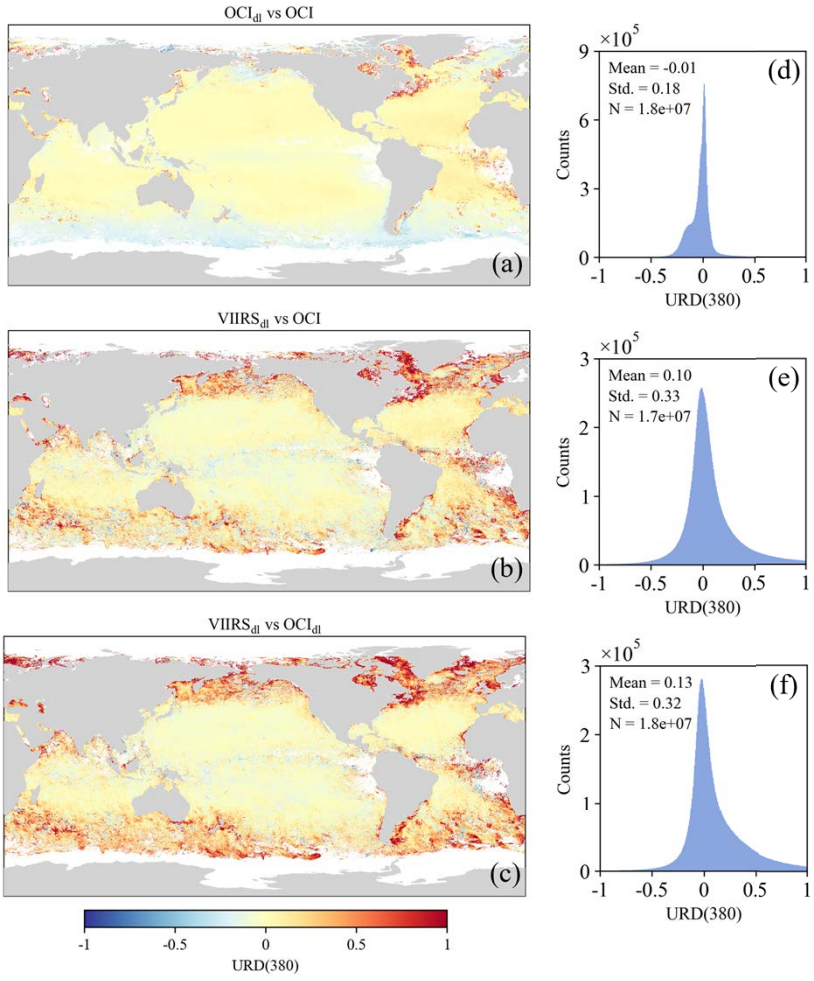

Fig. 4. Global distribution (left) and corresponding histogram (right) of URD(380) of global waters obtained from monthly satellite composite images of September 2024, comparing (a) modeled OCI_{dl} vs measured OCI, (b) modeled $VIIRS_{dl}$ vs measured OCI, and (c) modeled $VIIRS_{dl}$ vs modeled OCI_{dl}. The histogram includes the mean value (denoted as "Mean") and the standard deviation (denoted as "Std.").

To verify whether regions with large URD(380) values originate from the visible bands, we take 410 nm as an example. The connection between URD in the visible and nbUV bands is illustrated in Fig. 5. As shown in the spatial distribution of URD(410) derived from VIIRS and

Optics EXPRESS

OCI (Fig. 5(a)), larger absolute URD values are found in coastal and mid- to high-latitude regions, while values approach zero in low-latitude and open ocean areas, exhibiting a pattern similar to that of URD(380) between $VIIRS_{dl}$ and OCI. These higher absolute values may result from the significant spatial variation in water properties in coastal and mid- to high-latitude regions. In addition, a relatively high R^2 value (0.71) between URD(380) and URD(410) is observed, although the scatter is somewhat dispersed (Fig. 5(b)), indicating a loose but evident linkage between discrepancies in the R_{rs}(visible) and R_{rs}(nbUV). These results emphasize that greater consistency in R_{rs}(visible) measurements contributes to more reliable R_{rs}(nbUV) values for the $UVISR_{dl}$ system.

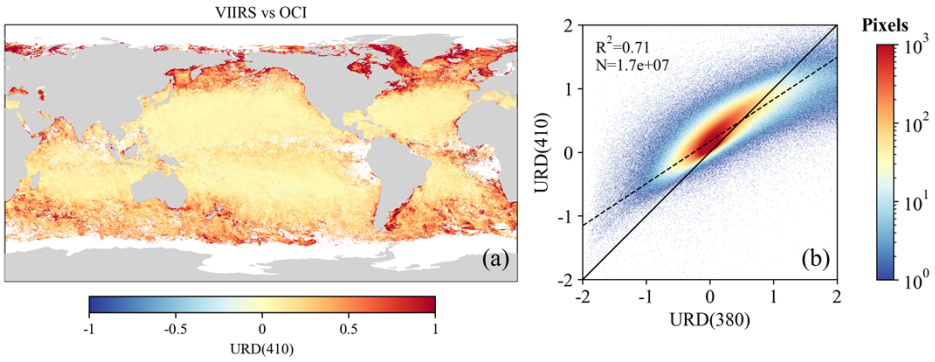

Fig. 5. (a) Global distribution of URD(410) between measured VIIRS and measured OCI of global waters obtained from monthly satellite composite images of September 2024. (b) Correlation plot showing the relationship between URD(380) ($VIIRS_{dl}$ vs OCI) and URD(410) (VIIRS vs OCI) for global waters, based on data from the same month.

In addition, we conducted a detailed analysis of regions with varying levels of consistency. Based on latitude (50° N/S) and depth (1000 m), the global ocean is categorized into four types: open ocean (depth > 1000 m), coastal (depth ≤ 1000 m), low-latitude (latitudes between 50°N and 50°S), and mid- to high-latitude (latitudes poleward of 50°N or 50°S). As shown in Table 1, deviations between $VIIRS_{dl}$ and OCI were relatively small in open ocean (MAURD ~0.14–0.27) and low-latitude regions (~0.13–0.25), but larger in coastal (~0.34–0.54) and mid- to high-latitude regions (~0.32–0.52), with consistency decreasing with decreasing wavelength across all regions. Clearly, the analysis demonstrates that regional differences, especially in coastal and mid- to high-latitude regions, highly influence the consistency of R_{rs}(nbUV) across different satellite sensors, highlighting the need to account for regional uncertainties when integrating multi-sensor satellite data.

The above analysis further confirms that the deviations between R_{rs}(nbUV) (especially for 380 and 400 nm) from $VIIRS_{dl}$ and OCI are more likely attributed to inter-sensor differences of R_{rs}(visible) rather than bias caused by the $UVISR_{dl}$ model; however, the latter's influence at 360 nm cannot be ignored. These conclusions are supported by the following three key findings: (1) Internal OCI vs OCI_{dl} comparisons show near-perfect agreement for R_{rs}(380) and R_{rs}(400), suggesting that minimal bias is introduced by the $UVISR_{dl}$ model itself especially for 380 and 400 nm wavelengths; (2) Visible-domain biases propagate into the nbUV range, as R_{rs}(nbUV) consistency patterns mirror those of R_{rs}(visible) with URD showing a strong correlation ($R^2 = 0.71$), and this bias cannot be ignored; (3) Larger R_{rs}(nbUV) inconsistencies between $VIIRS_{dl}$ and OCI or (OCI_{dl}) occur mainly in coastal and high-latitude regions, while internal OCI vs OCI_{dl} inconsistencies remain minor, indicating that strong spatial variabilities of water properties drive these deviations rather than the $UVISR_{dl}$ model.

Optics EXPRESS

Table 1. Accuracy assessment metrics for R_{rs}(nbUV) of $VIIRS_{dl}$ vs OCI across different oceanic regions and wavelengths. "open ocean" refers to areas with bottom depth > 1000 m, "coastal" to areas with bottom depth ≤ 1000 m, "low-latitude" to regions between 50°N and 50°S, and "mid- to high-latitude" to regions poleward of 50°N or 50°S.

Dataset	Location	Band (nm)	R^2	RMSD (sr^{-1})	bias (sr^{-1})	MAURD
$VIIRS_{dl}$ vs OCI		360	0.84	0.0023	1.1×10^{-3}	0.27
	open ocean	380	0.88	0.0017	2.6×10^{-4}	0.17
		400	0.91	0.0015	-8.4×10^{-5}	0.14
		360	0.86	0.0021	1.0×10^{-3}	0.25
	low-latitude	380	0.90	0.0016	1.9×10^{-4}	0.16
		400	0.92	0.0014	-2.2×10^{-4}	0.13
		360	0.72	0.0021	8.3×10^{-4}	0.54
	coastal	380	0.81	0.0016	5.1×10^{-4}	0.47
		400	0.84	0.0014	3.5×10^{-4}	0.34
		360	0.51	0.0027	9.9×10^{-4}	0.52
	mid- to high-latitude	380	0.63	0.0021	6.8×10^{-4}	0.41
		400	0.68	0.0018	7.2×10^{-4}	0.32

4.3. R_{rs}(380) among VIIRS, OCI, and SGLI

Since SGLI provides R_{rs}(380), it was further included to evaluate the consistency of R_{rs}(380) among VIIRS, OCI, and SGLI. Figure 6 shows the relationships between the R_{rs}(380) measured by SGLI and OCI, while Fig. 7 presents the corresponding relationships at visible bands. Similar to the procedure applied to VIIRS, the SGLI data from the monthly composite images of September 2024 were converted to 410, 440, 490, 550, and 670 nm using an empirical model.

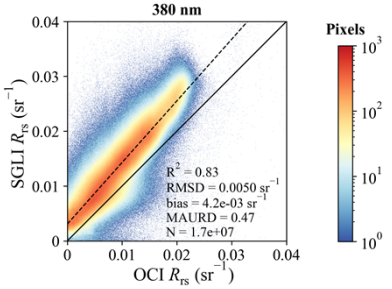

Fig. 6. Correlation plots between measured SGLI R_{rs}(380) and measured OCI R_{rs}(380) of global waters obtained from monthly satellite composite images of September 2024.

The comparisons revealed wavelength-associated patterns in agreement. Specifically, at 380 nm, a systematic positive bias in SGLI R_{rs} was observed, with a mean bias of approximately 0.0042 sr^{-1}. This is supported by the linear regression ($R^2 = 0.83$), whose fitted line lies above the 1:1 line (Fig. 6), with a slope of 1.12 and an intercept of 0.0031 sr^{-1}. Similar patterns can be observed when comparing SGLI R_{rs}(380) with that of OCI_{dl} and $VIIRS_{dl}$, where the bias values are ~0.004 sr^{-1}. The consistent patterns from different comparisons provide strong evidence that the discrepancies stem primarily from the SGLI R_{rs}(380) product, rather than from potential inaccuracies in the R_{rs}(nbUV) produced by the $UVISR_{dl}$. Meanwhile, as illustrated in Fig. 7, R_{rs} in the visible wavelengths (410–670 nm) show better inter-sensor consistency than R_{rs}(nbUV), as measured by MAURD. The R^2 values range from 0.75–0.87 and are comparable to those in the

Optics EXPRESS

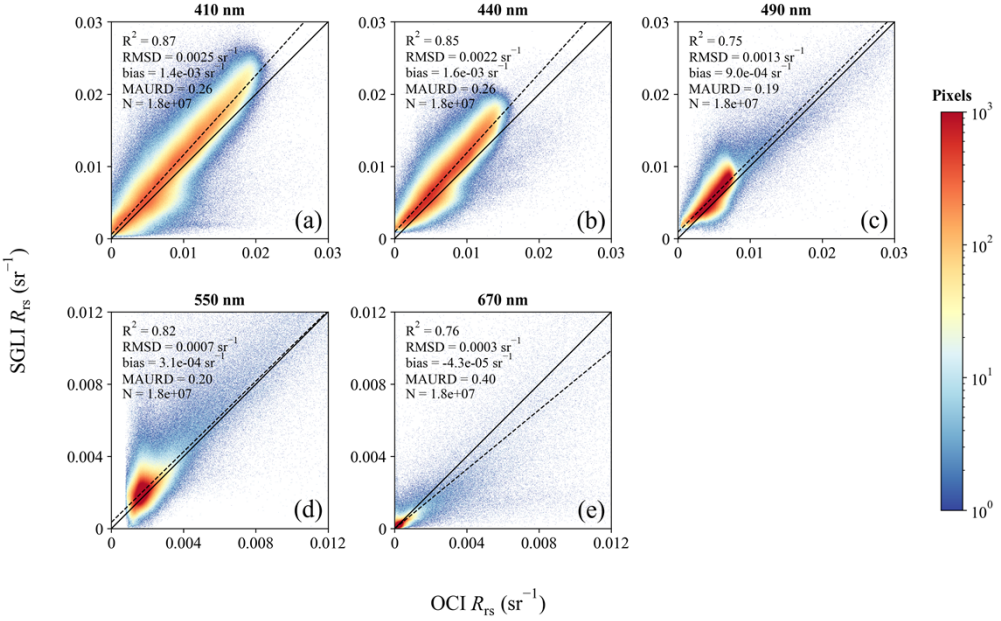

Fig. 7. Correlation plots between the SGLI R_{rs}(visible) and OCI R_{rs}(visible) for global waters obtained from monthly satellite composite images of September 2024.

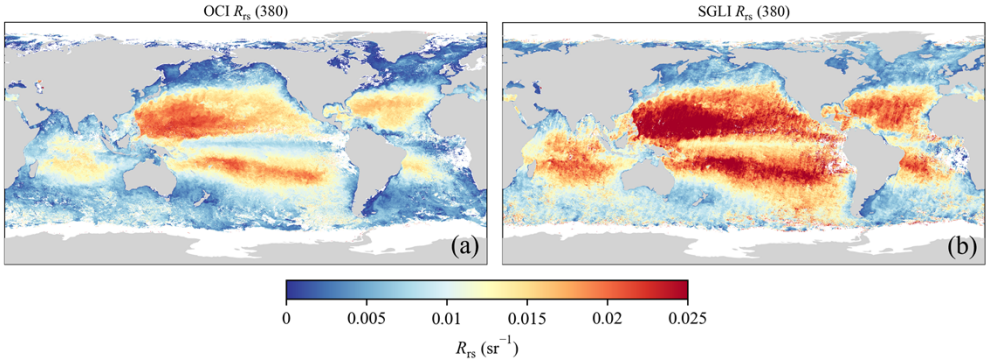

Fig. 8. Global distribution of (a) OCI-measured and (b) SGLI-measured R_{rs}(380) of global waters for September 2024.

nbUV bands, while the MAURD values remain below 0.26 across these bands, except at 670 nm, where low signal intensity amplifies relative differences (MAURD = 0.40). Notably, while a high degree of alignment was found between VIIRS and OCI (Fig. 2), SGLI demonstrates lower consistency with OCI, possibly due to higher uncertainties in the R_{rs} products of SGLI, which may stem from the relatively lower signal-to-noise ratio (SNR) at 380 nm [38,39], challenges in atmospheric correction [39], and unresolved issues in radiometric calibration [40].

The greater deviation in SGLI R_{rs}(380) is further evidenced by both the spatial distribution map (Fig. 8) and the comparative URD(380) analyses with OCI and VIIRS$_{dl}$ (Fig. 9). As shown in Fig. 8, the spatial distribution of SGLI R_{rs}(380) exhibits generally higher values than OCI, with extensive areas exceeding 0.025 sr^{-1}, which is significantly higher than typically observed in global oligotrophic waters. In addition, the URD(380) between SGLI and OCI (Figs. 9(a) and 9(c)) exhibits a spatial distribution pattern comparable to that between VIIRS$_{dl}$ and OCI

Optics EXPRESS

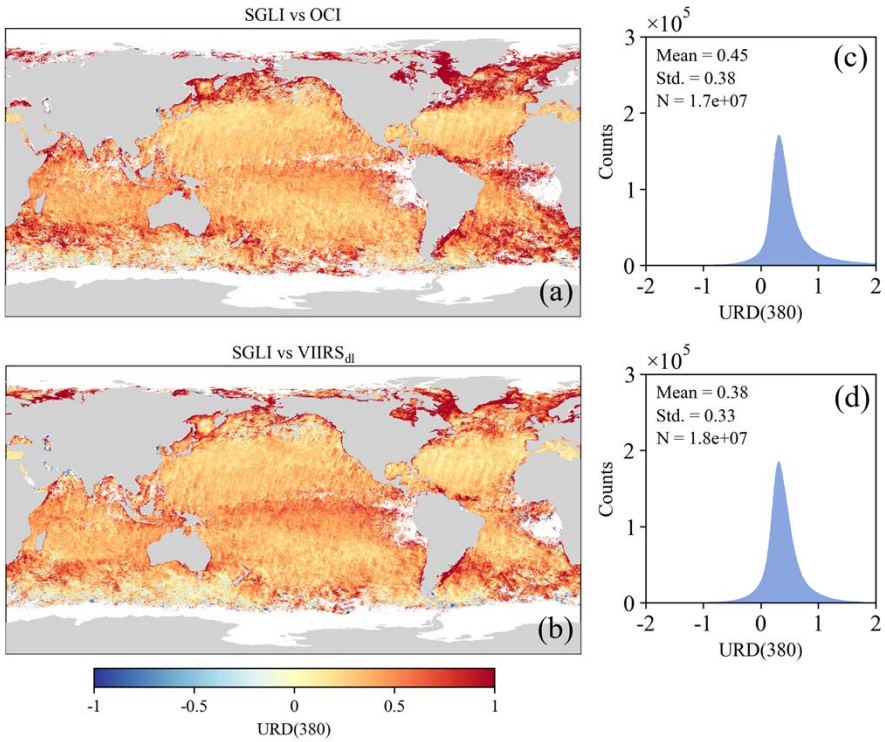

Fig. 9. Spatial distribution (left) and corresponding histogram (right) of URD(380) of global waters for September 2024, with (a) measured SGLI vs measured OCI and (b) measured SGLI vs modeled $VIIRS_{dl}$.

(Figs. 4(b) and 4(e)), with both showing lower values in open ocean waters and higher values in coastal and high-latitude regions. However, the URD(380) between SGLI and OCI has a higher overall mean (0.45) and a larger standard deviation (0.38). A comparable spatial pattern is also observed in the URD(380) between SGLI and $VIIRS_{dl}$ (Figs. 9(b) and 9(d)), with slightly lower values: a mean of 0.38 and a standard deviation of 0.33. Notably, URD(380) values in the open ocean generally lie between –0.22 and 1.04 (corresponding to two standard deviations around the mean), whereas in coastal regions they span a much broader interval from 0.51 to 2.00, with $R_{rs}(380)$ values often below 0.005 sr^{-1}, and over 8% of the URD(380) values for SGLI vs OCI exceed 100% versus 3% for $VIIRS_{dl}$ vs OCI.

Given the observed deviations, it can be inferred that SGLI $R_{rs}(380)$ may be subject to certain accuracy limitations, pointing to the necessity of further sensor calibration or algorithm refinements to achieve more reliable R_{rs} data.

4.4. *Comparison with in-situ measurements*

While it is found that the consistency between SGLI and OCI was weaker than that between VIIRS and OCI for R_{rs}(nbUV), it is necessary to compare R_{rs} from all three satellites with *in situ* observations to determine which sensor provides more accurate measurements and to verify the speculation in Section 4.3 that SGLI shows lower accuracy compared to OCI. For this purpose, satellite Level-2 products from VIIRS, OCI, and SGLI were compared with *in situ* measurements obtained from MOBY and AERONET-OC. MOBY R_{rs} data at the satellite wavelengths were used, while R_{rs} from AERONET-OC were converted to satellite bands (see Section 2 for details). The MOBY dataset, representative of clear open ocean waters, and the AERONET-OC dataset,

Optics EXPRESS

consisting of quality-assured R_{rs} data from coastal and optically complex waters, were used for this comparison.

We conducted comparisons of R_{rs}(nbUV) between satellite sensors (OCI and SGLI) and *in situ* measurements. This analysis was limited to MOBY data, as AERONET-OC provides only a single UV band at 400 nm and has insufficient matchup data for evaluation. As depicted in Fig. 10, in the nbUV bands, consistency between OCI and MOBY improves with increasing wavelength, reflected by decreasing MAURD values (0.21, 0.13, and 0.10, respectively). In the 380 nm band, OCI exhibits higher consistency with MOBY data compared to SGLI, whereas SGLI shows notably wider oscillations in R_{rs}(380), with a MAURD of 0.30 and a bias of 0.0018 sr^{-1}. A further analysis of the temporal trends between the three sensors from May to December 2024 revealed that the variability was uniformly distributed throughout the observation period.

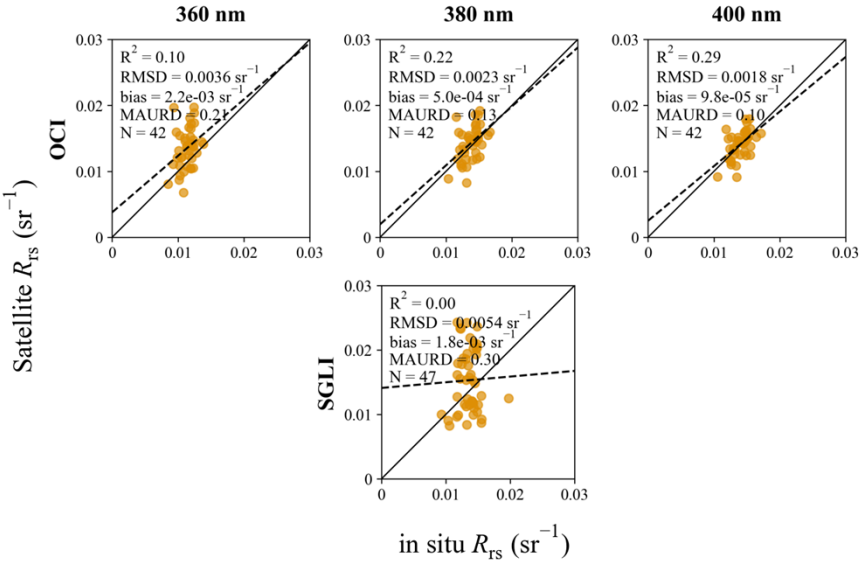

Fig. 10. Comparison between satellite-measured (OCI and SGLI) and *in situ* R_{rs}(nbUV) values for the period from May to December 2024.

Further, visible bands from AERONET-OC and MOBY (approximately at 410, 440, 490, 550, and 670 nm) were used to evaluate the accuracy of R_{rs}(visible) from OCI, VIIRS, and SGLI, thereby examining its differences to uncertainties of R_{rs}(nbUV) and the potential impact on $UVISR_{dl}$-derived R_{rs}(nbUV). Despite differences in the number of matched points, the OCI, VIIRS, and SGLI exhibit fair consistency with *in situ* data, with MAURD values ranging from 0.14 to 0.35 for the bands around 440, 490, and 550 nm. However, the MAURD values of SGLI R_{rs} are much higher for the wavelength of 412 nm, reaching up to 0.60, compared to approximately 0.34–0.35 for both OCI and VIIRS (Fig. 11). For the red band, SGLI shows better performance than OCI, with MAURD values of 0.37 and 0.53, respectively. This indicates that SGLI performs comparably to other satellites in the visible bands, with noticeably poorer performance only in the shorter wavelengths (nbUV and 412 nm bands). This further confirms the need for enhanced reliability of SGLI measurement at shorter wavelengths, as noted by Salem et al. [39]. Moreover, the relatively larger deviation of SGLI R_{rs} at 412 nm may propagate into the $UVISR_{dl}$-derived R_{rs}(nbUV), thereby impacting its consistency with results from OCI and VIIRS.

Optics EXPRESS

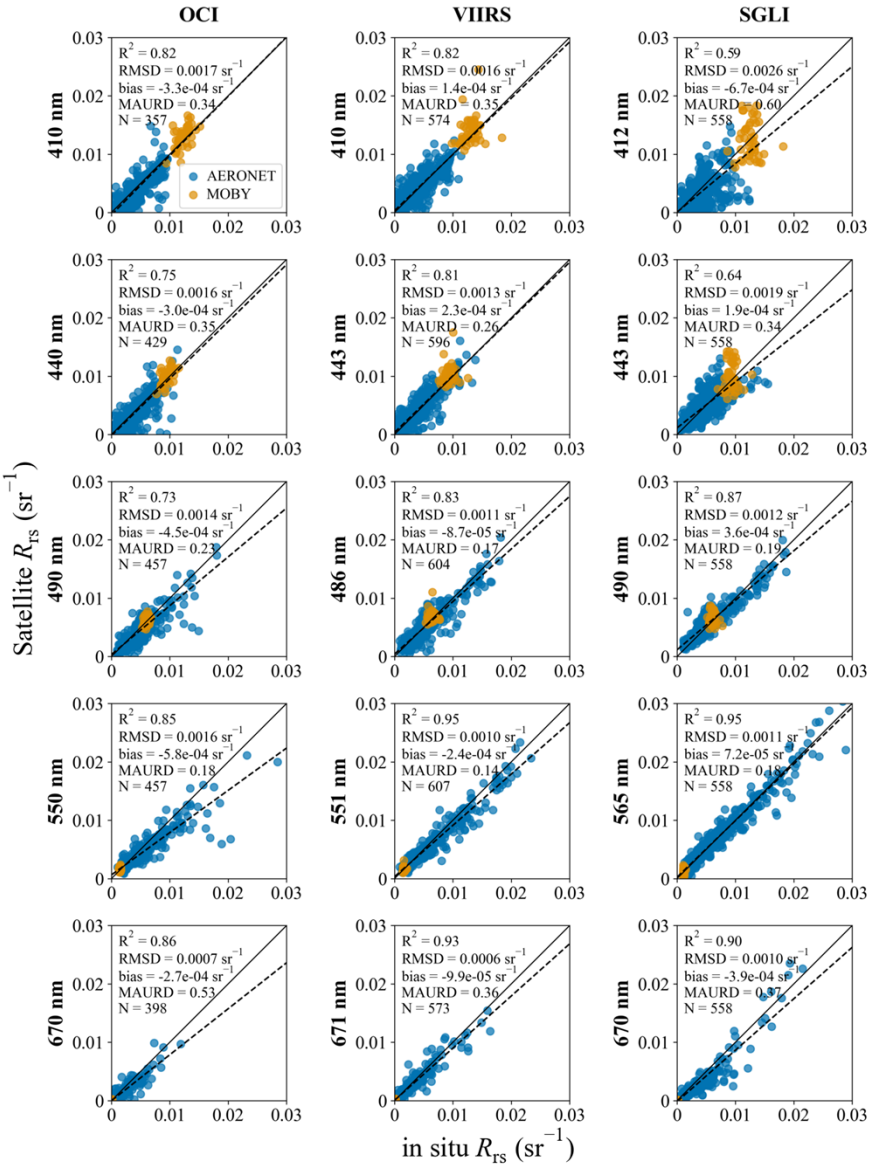

Fig. 11. Comparison between satellite-measured (VIIRS, OCI, and SGLI) and *in situ* R_{rs}(visible) values for the period from May to December 2024.

Optics EXPRESS

5. Discussion

The results presented in this study demonstrate that $UVISR_{dl}$ has the potential to bridge the temporal gap in satellite-derived R_{rs}(nbUV) data, as it enables the reconstruction of historical records of R_{rs}(nbUV) over the past few decades. By leveraging direct measurements from SGLI and OCI in the 360–400 nm range, we confirmed that the proposed deep-learning model provides R_{rs}(nbUV) estimations with high inter-sensor consistency and low uncertainty for global oceanic waters. These outcomes align with the performance reported in $UVISR_{dl}$'s initial validation using VIIRS, MODIS, and SeaWiFS data [25], reinforcing its generalizability across sensors and regions. The following sections explore the main influences on R_{rs}(nbUV) consistency across satellites, its correlation with visible bands, and the potential applications of $UVISR_{dl}$ in ocean color remote sensing.

5.1. Factors affecting the consistency of R_{rs}(nbUV) across satellite sensors

Based on the results of this study, we observed that the consistency of R_{rs} in the nbUV generally decreases at shorter wavelengths. This reduction in consistency can be attributed to satellite-specific uncertainties and inter-sensor differences.

Prior studies have highlighted a few dominant contributors to R_{rs} uncertainty (u_c; unit: sr^{-1}), including random sensor noise, systematic calibration errors, and forward model assumptions [41]. These intrinsic factors are especially pronounced in the UV range and tend to amplify in regions of greater optical complexity. Figure 12 illustrates this by comparing the mean R_{rs} values along with their corresponding mean u_c and relative uncertainty δ ($u_c/R_{rs} \times 100$; unit: %) for two distinctly different sites: MOBY, located in the open ocean near Hawaii, and MVCO (one of the AERONET-OC sites), situated in coastal waters off the eastern coast of the United States. The R_{rs} and associated u_c values at MOBY and MVCO were extracted from the PACE OCI Level-2 data, in which both are provided by default as part of the standard Level-2 OC product suite (additional references can be found in Zhang et al. [41,42]). For both MOBY and MVCO, u_c is found to increase exponentially with decreasing wavelength, from values near zero at 719 nm to over 0.0013 sr^{-1} at around 350 nm. Slightly higher u_c values are recorded at the coastal site MVCO compared to the open ocean site MOBY. Due to the extremely low R_{rs} values in the nbUV at MVCO, the relative uncertainty is significantly amplified, resulting in values that are approximately an order of magnitude higher than those observed at MOBY (Fig. 12(c)).

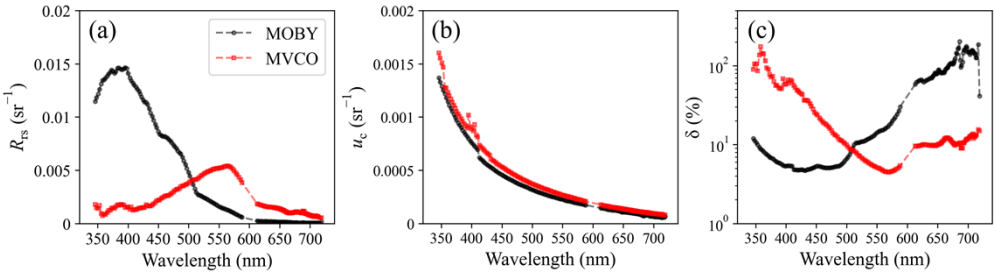

Fig. 12. Spectral mean OCI R_{rs} (a) along with its associated absolute uncertainty u_c (b) and relative uncertainty δ ($u_c/R_{rs} \times 100$) (c) at MOBY and AERONET site MVCO during the period from May to December 2024.

The precision of atmospheric correction directly affects R_{rs} measurements. Aerosols and Rayleigh scattering represent two major uncertainty sources in atmospheric correction processes. Current aerosol correction methods for NASA ocean color satellite sensors [43,44] or GCOM-C SGLI [45,46] are built upon the framework established by Gordon and Wang [47], which employs near-infrared (NIR) or shortwave infrared (SWIR) bands to estimate aerosol contributions

Optics EXPRESS

and extrapolate them to UV-blue wavelengths. However, as the IOCCG Report No. 10 [48] demonstrated, extrapolating aerosol properties to shorter wavelengths becomes increasingly error-prone.

Further, retrieving accurate R_{rs} at shorter wavelengths is inherently challenging due to the relatively weaker water-leaving signals compared to the dominant atmospheric contributions. In the nbUV, the sharp decline in solar irradiance coupled with enhanced atmospheric Rayleigh scattering, whose intensity is proportional to λ^{-4}, amplifies this imbalance; for instance, Rayleigh radiance at 350 nm is approximately 16 times that at 700 nm [10]. Moreover, as reported by Wang [49], radiative transfer simulations across 340–2130 nm for several black ocean cases show that Rayleigh scattering dominates the nbUV top-of-atmosphere reflectance (>90% at 340 nm). Consequently, even minor inaccuracies in Rayleigh radiance removal can substantially inflate relative errors of R_{rs} in the nbUV [12]. Wang [50] also showed that variations in surface atmospheric pressure, directly influencing Rayleigh optical thickness, could induce measurable radiance biases: a ± 3% pressure variation yields about 0.2% error in Rayleigh radiance at 412 nm, causing 2–5% uncertainty in R_{rs}; this effect is expected to be even more pronounced in the nbUV, where Rayleigh contributions are higher. Such pressure-induced biases are particularly relevant in regions where atmospheric pressure significantly deviates from the standard pressure (1013.25 hPa), such as polar areas and high-altitude inland waters; thus, ignoring dynamic atmospheric pressure variations can systematically bias R_{rs}(nbUV) measurements.

Furthermore, sensor performance limitations exacerbate uncertainties in R_{rs}(nbUV). Ocean color sensors generally exhibit lower SNR at UV wavelengths due to decreased solar irradiance and reduced detector sensitivity [10]. For instance, the GCOM-C SGLI sensor exhibits notably lower SNR in its 380 nm channel (~650) compared to visible wavelengths, which exceed 1000 at 565 nm [38]. Calibration difficulties in the UV are further compounded by limited stable and accurate radiometric reference sources. The AERONET-OC network, predominantly supporting visible wavelengths, offers limited capability in UV calibration. Additionally, inter-sensor variability arises due to differences in instrument designs and calibration approaches among satellite platforms (e.g., OCI, SGLI, VIIRS), further contributing to inconsistencies in nbUV data as highlighted in Section 4.

In summary, satellite-specific factors, including atmospheric correction inaccuracies and inherent sensor noise, combined with inter-sensor differences (e.g., temporal-spatial coverage variations, resolution differences, and instrument characteristics), primarily drive the lower consistency observed in R_{rs}(nbUV). Addressing these uncertainties through enhanced atmospheric correction techniques and improved sensor calibration processes will be crucial for ensuring greater compatibility among satellite-derived ocean color datasets.

5.2. Relative relationship of R_{rs} between UV bands and VIS bands

In the past, several studies have explored the complex and nonlinear relationship between R_{rs}(nbUV) and R_{rs}(visible), employing simulated data [25,26], *in situ* measurements [25,26,51], as well as satellite observations [21]. These studies highlight the complexity of optical interactions in coastal and open ocean waters. A common finding is the emergence of a two-cluster pattern in the relationship between R_{rs}(nbUV) and R_{rs}(visible), reflecting relative differences in $a_g(\lambda)$ and $a_{ph}(\lambda)$, with $a_g(\lambda)$ dominating in the UV bands and $a_{ph}(\lambda)$ dominating the blue wavelengths.

Building on this foundation, the present study further investigated the relationship between nbUV and visible bands by analyzing $R_{rs}(380)/R_{rs}(442)$ ratios, following the approaches of Wang et al. [21], Wang et al. [25], and Liu et al. [26]. This analysis included correlation plots between $R_{rs}(380)$ and $R_{rs}(442)$ (or $R_{rs}(443)$) (Fig. 13) as well as the spatial distribution of the $R_{rs}(380)/R_{rs}(442)$ ratio (Fig. 14).

As shown in Figs. 13(a)–13(c), a persistent two-cluster pattern is observed across data sources (OCI and VIIRS) and retrieval methods (observation-based or $UVISR_{dl}$-derived), characterized

Optics EXPRESS

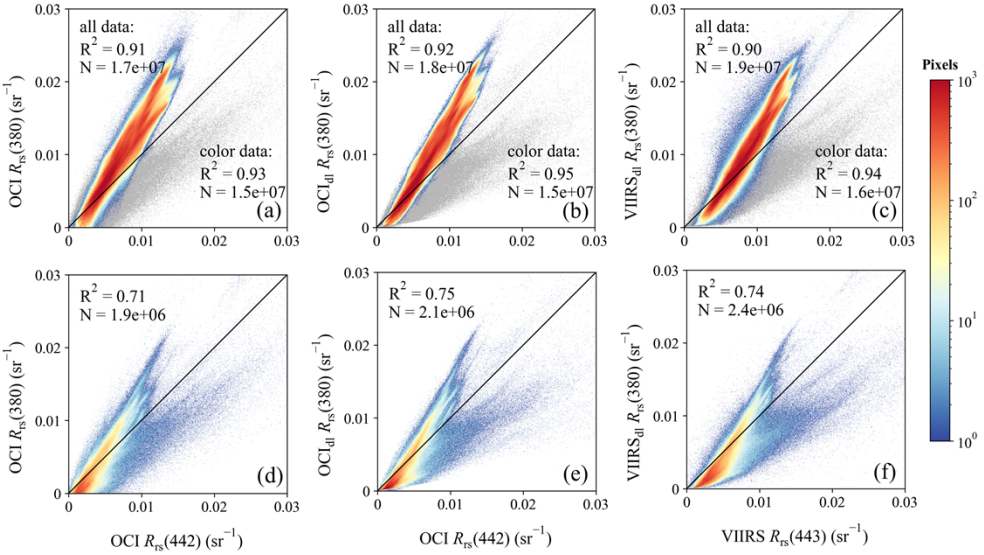

Fig. 13. Correlation plots between $R_{rs}(380)$ and $R_{rs}(442)$ (or $R_{rs}(443)$) derived from $UVISR_{dl}$ outputs and satellite observations, based on monthly composite images of September 2024. Panels (a–c) show OCI $R_{rs}(380)$ vs OCI $R_{rs}(442)$, OCI_{dl} $R_{rs}(380)$ vs OCI $R_{rs}(442)$, and $VIIRS_{dl}$ $R_{rs}(380)$ vs VIIRS $R_{rs}(443)$ for global waters ("all data"); colored points denote data with bottom depth >1000 m ("color data"), while grey points denote data with bottom depth ≤ 1000 m. Panels (d–f) show the same comparisons as (a–c), but restricted to the grey subset (bottom depth ≤ 1000 m).

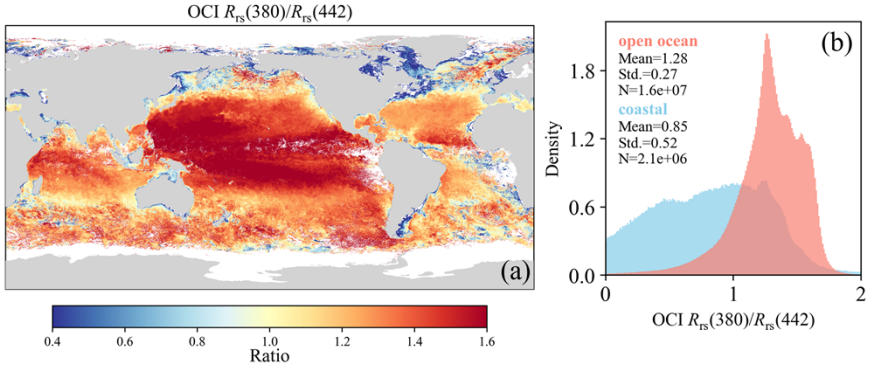

Fig. 14. (a) Spatial distribution of the $R_{rs}(380)/R_{rs}(442)$ ratio of global waters obtained from monthly satellite composite images of September 2024, and (b) corresponding histograms for pixels in open ocean and coastal areas, respectively.

by the separation of data points into two groups when comparing $R_{rs}(380)$ and $R_{rs}(442)$. In particular, for the same $R_{rs}(442)$, higher $R_{rs}(380)/R_{rs}(442)$ ratios are primarily found in open ocean regions, while lower values occur in coastal areas, with the 1000 m isobath serving as a general boundary following Wang et al. [25]. This consistent pattern demonstrates that $UVISR_{dl}$ effectively captures this nonlinear relationship. Moreover, this pattern aligns with the earlier studies [21,25], demonstrating its universality.

However, although we roughly delineated the two patterns using the isobath, they cannot be clearly separated based solely on this boundary. In regions where the depth > 1000 m, the waters

Optics EXPRESS

are predominantly open ocean and are typically considered as "Case-1" [13,52], although this concept was not defined based on location or values of chlorophyll concentration [53,54]. The optical properties in "Case-1" waters are primarily governed by phytoplankton, with relatively low influence from CDOM and suspended particles. Compared to global waters, these waters exhibit a relatively stronger linear correlation between $R_{rs}(380)$ and $R_{rs}(442)$. As shown in Fig. 13(a), excluding coastal data points improves the R^2 value from 0.91 to 0.93 and reduces the MAURD between the OCI $R_{rs}(380)$ and the linear regression line (fitted using $R_{rs}(380)$ and $R_{rs}(442)$) from 0.31 to 0.29. The OCI $R_{rs}(380)/R_{rs}(442)$ ratio in these waters has a mean of 1.28 and a standard deviation of 0.27 (Fig. 14(b)). This relatively strong relationship suggests that phytoplankton influences both nbUV and blue wavelengths.

In contrast, as illustrated in Figs. 13(d)–13(f), a two-cluster pattern is also present in coastal regions where the depth ≤ 1000 m. Moreover, the remarkably consistent pattern observed across all three panels in Figs. 13(d)–13(f) indicates that the two-cluster feature in coastal regions is consistently captured between OCI and VIIRS. In such regions with bottom depth ≤ 1000 m, the OCI $R_{rs}(380)/R_{rs}(442)$ ratio has a lower mean of 0.85 and a larger standard deviation of 0.52 (Fig. 14(b)), and the spatial distribution of this ratio, exemplified by OCI data (Fig. 14(a)), appears highly scattered and lacks a clear geographic boundary, making it difficult to separate the clusters based solely on location. This further implies that the relationships between R_{rs}(nbUV) and R_{rs}(visible) are rather complex, especially in optically complex coastal environments.

This raises the question: Can R_{rs}(nbUV) be reliably estimated simply based on the published global empirical relationships? This proves extremely complex due to two main reasons: first, the "Case-1" bio-optical relationships break down in the nbUV domain, primarily because of the weak correlation between CDOM and pigment content, as well as the influence of specific UV-absorbing substances such as MAAs [8,55]. In nearshore turbid waters, multiple constituents interact nonlinearly, further decoupling the responses of nbUV and the visible band [56]. Second, water-type classifications are ambiguous. Such as the "Case-1" and "Case-2" classifications [57] cannot be determined solely by chlorophyll concentration or geography, and remote sensing alone cannot reliably distinguish them well [53]. These limitations highlight the need for alternative advanced methods, which have been demonstrated to more effectively capture complex nonlinear relationships across various aquatic environments [25,26,58].

5.3. Application prospects of UVISR$_{dl}$ in ocean color remote sensing

In this study, the feasibility of the $UVISR_{dl}$ system is successfully demonstrated using the data from OCI (Section 3.2), highlighting its strong generalization capability. This approach shows promise for achieving R_{rs}(nbUV) with high consistency for multiple satellites. To further illustrate the advantages of this system, this study further tests the $UVISR_{dl}$ system using SGLI data. As shown in Section 4.3, the consistency between SGLI and OCI (or VIIRS) is relatively poor, particularly at 380 nm, where R_{rs} values from SGLI are systematically higher, with the MAURD between SGLI and OCI reaching up to 0.47 (Fig. 6(a)). In contrast, the visible bands show considerably better agreement, with MAURD values between SGLI and OCI remaining below 0.26 across the 410–550 nm range (Figs. 7(a)–(d)). Therefore, deriving $R_{rs}(380)$ by $UVISR_{dl}$ may help reduce the deviation associated with the SGLI 380 band. As expected, the results show that the consistency between $SGLI_{dl}$ and OCI $R_{rs}(380)$ (Fig. 15(b)) is much better than that between SGLI and OCI $R_{rs}(380)$ (Fig. 6(a)). This is supported by a lower RMSD (0.0026 sr^{-1} vs 0.005 sr^{-1}), lower bias (0.00074 sr^{-1} vs 0.0042 sr^{-1}), and lower MAURD (0.29 vs 0.47). In addition, the $R_{rs}(360)$ and $R_{rs}(400)$ produced by $UVISR_{dl}$ also show reasonable agreement with the corresponding bands of OCI (Figs. 15(a) and 15(c)). For $R_{rs}(360)$, the R^2 value is 0.77 and the MAURD is 0.35. $R_{rs}(400)$ exhibits better agreement, with the highest R^2 of 0.87 and the lowest MAURD of 0.25 among the three bands. In addition to satellite intercomparison, *in situ* validation has been tested further. Based on the matchups with MOBY $R_{rs}(380)$, $SGLI_{dl}$ $R_{rs}(380)$

Optics EXPRESS

also has a smaller bias compared to SGLI $R_{rs}(380)$, with the RMSD reduced from 0.0054 to 0.0042 sr^{-1} and the bias reduced from 0.0018 to -0.0004 sr^{-1}.

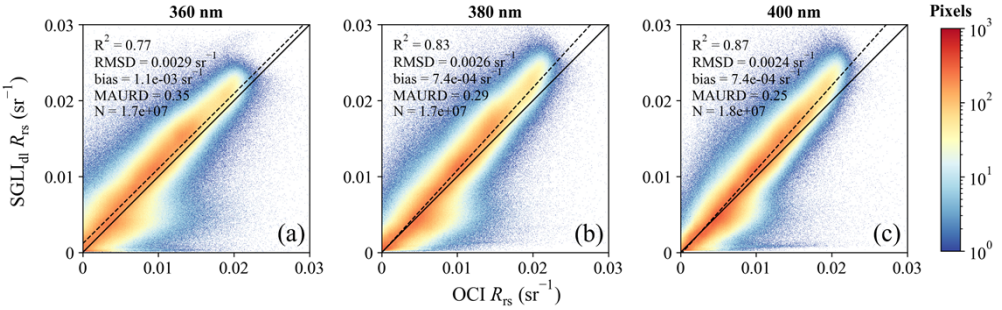

Fig. 15. Correlation plots between modeled $SGLI_{dl}$ R_{rs}(nbUV) vs measured OCI R_{rs}(nbUV) of global waters obtained from monthly satellite composite images of September 2024.

Furthermore, a comparison of the global distributions of URD(380) of SGLI vs OCI (Fig. 9(a)) and $SGLI_{dl}$ vs OCI (Fig. 16(a)) reveals that areas where SGLI previously exhibited a clear positive bias relative to OCI have become more consistent after applying $UVISR_{dl}$. The mean URD(380) decreased markedly from 0.45 to 0.04, although the standard deviation increased slightly by 5%, indicating a significant overall improvement in the consistency between SGLI and OCI for $R_{rs}(380)$.

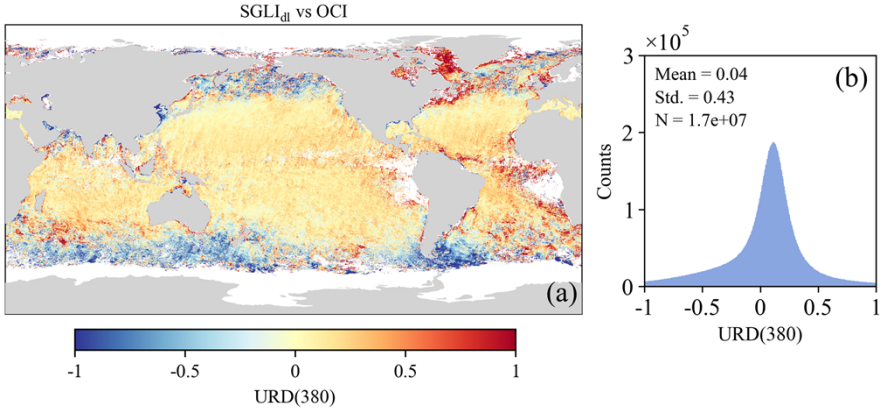

Fig. 16. Spatial distribution of URD(380) between modeled $SGLI_{dl}$ and measured OCI (a) and corresponding histogram (b) of global waters obtained from monthly satellite composite images of September 2024.

Consistent with the regional accuracy analysis in Table 1, the improvements are particularly evident in the open ocean and low-latitude regions, as shown in Table 2. Specifically, the MAURD in the open ocean slightly decreased from 0.43 to 0.26, and in the low-latitude region, it dropped from 0.43 to 0.23. In addition, the $SGLI_{dl}$-derived $R_{rs}(360)$ and $R_{rs}(400)$ bands also exhibit comparable accuracy in these regions, with MAURD values of 0.32 and 0.22 in the open ocean, and 0.29 and 0.20 in the low-latitude region, respectively. These results support the effectiveness of the $UVISR_{dl}$ approach in improving consistency with OCI's R_{rs}(nbUV).

Together, based on the performance of $UVISR_{dl}$ on SGLI data, we conclude that an application of $UVISR_{dl}$ is not only effective in improving inter-sensor consistency for R_{rs}(nbUV) but also flexible enough to be extended to other nbUV wavelengths. Importantly, although the model

Optics EXPRESS

Table 2. Accuracy assessment metrics for R_{rs}(nbUV) of (a) SGLI vs OCI, and (b) SGLI$_{dl}$ vs OCI across different oceanic regions and wavelengths. "Open ocean" refers to areas with bottom depth > 1000 m, "coastal" to areas with bottom depth ≤ 1000 m, "low-latitude" to regions between 50 °N and 50 °S, and "mid- to high-latitude" to regions poleward of 50 °N or 50 °S.

Dataset	Location	Band (nm)	R^2	RMSD (sr^{-1})	bias (sr^{-1})	MAURD
(a): SGLI vs OCI	open ocean	380	0.81	0.0051	4.3×10^{-3}	0.43
	low-latitude	380	0.83	0.0052	4.5×10^{-3}	0.43
	coastal	380	0.65	0.0039	3.0×10^{-3}	0.83
	mid- to high-latitude	380	0.39	0.0039	2.6×10^{-3}	0.67
(b): SGLI$_{dl}$ vs OCI		360	0.76	0.0029	1.2×10^{-3}	0.32
	open ocean	380	0.82	0.0027	8.4×10^{-4}	0.26
		400	0.86	0.0024	8.6×10^{-4}	0.22
		360	0.81	0.0028	1.5×10^{-3}	0.29
	low-latitude	380	0.85	0.0026	1.1×10^{-3}	0.23
		400	0.87	0.0023	1.1×10^{-3}	0.20
		360	0.57	0.0025	7.3×10^{-5}	0.61
	coastal	380	0.67	0.0022	-1.7×10^{-5}	0.54
		400	0.69	0.0020	-6.8×10^{-5}	0.47
		360	0.22	0.0035	-1.0×10^{-3}	0.64
	mid- to high-latitude	380	0.32	0.0030	-9.5×10^{-4}	0.57
		400	0.39	0.0024	-6.3×10^{-4}	0.47

was originally developed only for deriving 360, 380, and 400 nm bands, it is also capable of generating R_{rs} data at other wavelengths within the nbUV range. This is because the training dataset is based on hyperspectral spectra, which provides greater spectral flexibility. Thus, it can help to resolve the issue of band mismatches commonly encountered in multi-satellite data fusion, and therefore demonstrates high adaptability across different satellite sensors, such as SeaWiFS and MODIS [25].

6. Summary and conclusion

This study conducted a series of evaluations regarding the UVISR$_{dl}$ system to 1) verify its global performance with R_{rs}(nbUV) from measurements by PACE OCI's UV bands; 2) evaluate the consistency of R_{rs}(nbUV) among VIIRS, OCI, and SGLI for inter-sensor validation, and 3) confirm whether the UVISR$_{dl}$ developed for a general 5-bands configuration (410, 440, 490, 550, and 670 nm) can be applied to other sensors such as OCI and SGLI.

The key findings include: (1) The modelled OCI R_{rs}(nbUV) from OCI R_{rs}(visible) exhibits very good consistency with its measured values, demonstrating a strong performance of the UVISR$_{dl}$ system. This result indicates that the UVISR$_{dl}$ system effectively captures the complex nonlinear relationships between UV R_{rs} and visible R_{rs}; (2) The R_{rs}(nbUV) from VIIRS and OCI exhibit generally good consistency, especially at 380 and 400 nm. Thus, it is reliable to extend satellite nbUV measurements back to the MODIS and VIIRS era; (3) Larger inter-satellite differences in R_{rs}(visible) bands will be propagated into R_{rs}(nbUV) during the UVISR$_{dl}$ process, suggesting that achieving high consistency in R_{rs}(nbUV) requires a correspondingly high level of consistency in R_{rs}(visible). This is especially true for polar region waters (north of 50 °N or south of 50 °S); (4) SGLI showed lower consistency than others, demonstrating a need for further calibration of SGLI in the UV band.

Optics EXPRESS

Looking forward, future efforts should focus on further improving the robustness of $UVISR_{dl}$ in high-latitude and coastal waters by incorporating high-quality R_{rs} data and ancillary UV-related parameters into the training process, expanding validation with more *in situ* data such as AERONET-OC, quantitatively attributing visible-to-UV error propagation through sensitivity analyses, and leveraging its spectral flexibility to apply across multiple sensors, including SeaWiFS and MODIS. In addition, retraining with real high-quality UV measurements will be ideal to optimize performance at the nbUV domain.

In summary, although the essential role of direct satellite UV measurements must be emphasized [21], this study demonstrates the feasibility and applicability of the $UVISR_{dl}$ system in estimating R_{rs}(nbUV) from R_{rs}(visible). It is anticipated that, with the generation of R_{rs}(nbUV) from sensors such as MODIS and VIIRS, more and improved ocean color products could be provided, which will not only contribute to advancing ocean color remote sensing but also help our understanding of long-term interactions between UV radiation and biogeochemical processes in the global ocean.

Funding. National Natural Science Foundation of China (42430107); National Key Research and Development Program of China (2022YFB3901703, 2022YFC3104903).

Acknowledgment. We are grateful for the financial support from the National Natural Science Foundation of China (#42430107), the National Key Research and Development Program of China (2022YFB3901703, 2022YFC3104903), Fujian Satellite Data Development, Co., Ltd., and Fujian Haisi Digital Technology Co., Ltd. We also acknowledge NASA for providing PACE-OCI and VIIRS-SNPP ocean color products, the SeaDAS software, and JAXA for providing GCOM-C/SGLI data, as well as the many AERONET-OC sites and the MOBY site for providing valuable measurements. Constructive comments and suggestions from two anonymous reviewers are greatly appreciated.

Disclosures. The authors declare no conflicts of interest.

Data availability. Data underlying the results presented in this paper are not publicly available at this time but may be obtained from the authors upon reasonable request.

References

1. C. Booth and J. Morrow, "The penetration of UV into natural waters," Photochem. Photobiol. **65**(2), 254–257 (1997).
2. P. E. Hockberger, "A History of Ultraviolet Photobiology for Humans, Animals and Microorganisms," Photochem. Photobiol. **76**(6), 561–579 (2002).
3. J. J. Cullen and P. J. Neale, "Ultraviolet radiation, ozone depletion, and marine photosynthesis," Photosynth. Res. **39**(3), 303–320 (1994).
4. M. A. Moran and R. G. Zepp, "Role of photoreactions in the formation of biologically labile compounds from dissolved organic matter," Limnology and Oceanography **42**(6), 1307–1316 (1997).
5. G. Herndl, J. Arrieta, E. Kaiser, *et al.*, "Role of ultraviolet radiation in aquatic systems: interaction between mixing processes, photochemistry and microbial activity," in *Microbial biosystems: new frontiers. Proceedings of the 8th International Symposium on Microbial Ecology*, (2000), 209–219.
6. D.-P. Häder, C. E. Williamson, S-Å Wängberg, *et al.*, "Effects of UV radiation on aquatic ecosystems and interactions with other environmental factors," Photochem. Photobiol. Sci. **14**(1), 108–126 (2014).
7. D.-P. Häder, E. W. Helbling, C. Williamson, *et al.*, "Effects of UV radiation on aquatic ecosystems and interactions with climate change," Photochem. Photobiol. Sci. **10**(2), 242–260 (2011).
8. J. M. Shick and W. C. Dunlap, "Mycosporine-like amino acids and related gadusols: biosynthesis, accumulation, and UV-protective functions in aquatic organisms," Annu. Rev. Physiol. **64**(1), 223–262 (2002).
9. R. Zepp, D. E. Iii, N. Paul, *et al.*, "Interactive effects of solar UV radiation and climate change on biogeochemical cycling," Photochem. Photobiol. Sci. **6**(3), 286–300 (2007).
10. C. R. McClain, G. Meister, and B. Monosmith, "Chapter 2.1 - Satellite Ocean Color Sensor Design Concepts and Performance Requirements," in *Experimental Methods in the Physical Sciences*, G. Zibordi, C. J. Donlon, and A. C. Parr, eds. (Academic Press, 2014), pp. 73–119.
11. IOCCG, "Ocean-colour observations from a geostationary orbit," (IOCCG, Dartmouth, Canada, 2012).
12. R. J. Frouin, B. A. Franz, A. Ibrahim, *et al.*, "Atmospheric correction of satellite ocean-color imagery during the PACE era," Front. Earth Sci. **7**, 145 (2019).
13. IOCCG, "Remote Sensing of Ocean Colour in Coastal and Other Optically Complex Waters," (IOCCG, Dartmouth, Canada, 2000).
14. X. He, Y. Bai, D. Pan, *et al.*, "Atmospheric correction of satellite ocean color imagery using the ultraviolet wavelength for highly turbid waters," Opt. Express **20**(18), 20754–20770 (2012).
15. A. Mannino, M. G. Novak, S. B. Hooker, *et al.*, "Algorithm development and validation of CDOM properties for estuarine and continental shelf waters along the northeastern US coast," Remote Sensing of Environment **152**, 576–602 (2014).

Optics EXPRESS

16. J. Wei, Z. Lee, M. Ondrusek, *et al.*, "Spectral slopes of the absorption coefficient of colored dissolved and detrital material inverted from UV-visible remote sensing reflectance," JGR Oceans **121**(3), 1953–1969 (2016).
17. J. R. Helms, A. Stubbins, J. D. Ritchie, *et al.*, "Absorption spectral slopes and slope ratios as indicators of molecular weight, source, and photobleaching of chromophoric dissolved organic matter," Limnol. Oceanogr. **53**(3), 955–969 (2008).
18. J. Wei and Z. Lee, "Retrieval of phytoplankton and colored detrital matter absorption coefficients with remote sensing reflectance in an ultraviolet band," Appl. Opt. **54**(4), 636–649 (2015).
19. N. Lamquin, S. Clerc, L. Bourg, *et al.*, "OLCI A/B Tandem Phase Analysis, Part 1: Level 1 Homogenisation and Harmonisation," Remote Sensing **12**(11), 1804 (2020).
20. Y. Okamura, T. Hashiguch, T. Urabe, *et al.*, "Pre-Launch Characterisation and In-Orbit Calibration of GCOM-C/SGLI," in *IGARSS 2018 - 2018 IEEE International Geoscience and Remote Sensing Symposium*, (2018), 6651–6654.
21. J. Wang, S. Chen, S. Hu, *et al.*, "System vicarious calibration and ocean color retrieval from the HY-1C UVI," International Journal of Applied Earth Observation and Geoinformation **136**, 104417 (2025).
22. G. Meister, J. J. Knuble, U. Gliese, *et al.*, "The Ocean Color Instrument (OCI) on the Plankton, Aerosol, Cloud, ocean Ecosystem (PACE) Mission: System Design and Prelaunch Radiometric Performance," IEEE Trans. Geosci. Remote Sensing **62**, 1–18 (2024).
23. J. L. Burley, S. T. Fiorino, B. J. Elmore, *et al.*, "A remote sensing and atmospheric correction method for assessing multispectral radiative transfer through realistic atmospheres and clouds," Journal of Atmospheric and Oceanic Technology **36**(2), 203–216 (2019).
24. R. E. Eplee Jr, J. W. McIntire, S. Lee, *et al.*, "Initial on-orbit spectral calibration of the PACE Ocean Color Instrument," in *Earth Observing Systems XXIX*, (SPIE, 2024), 194–205.
25. Y. Wang, Z. Lee, J. Wei, *et al.*, "Extending satellite ocean color remote sensing to the near-blue ultraviolet bands," Remote Sensing of Environment **253**, 112228 (2021).
26. H. Liu, X. He, Q. Li, *et al.*, "Estimating ultraviolet reflectance from visible bands in ocean colour remote sensing," Remote Sensing of Environment **258**, 112404 (2021).
27. D. Clark, H. Gordon, K. Voss, *et al.*, "Validation of atmospheric correction over the oceans," J. Geophys. Res. **102**(D14), 17209–17217 (1997).
28. G. Zibordi, B. Holben, S. B. Hooker, *et al.*, "A network for standardized ocean color validation measurements," EoS Transactions **87**(30), 293–297 (2006).
29. R. A. Vandermeulen, R. Arnone, S. Ladner, *et al.*, "Enhanced satellite remote sensing of coastal waters using spatially improved bio-optical products from SNPP–VIIRS," Remote Sensing of Environment **165**, 53–63 (2015).
30. A. Wu, X. Xiong, R. Bhatt, *et al.*, "An Assessment of SNPP and NOAA20 VIIRS RSB Calibration Performance in NASA SIPS Reprocessed Collection-2 L1B Data Products," Remote Sensing **14**(17), 4134 (2022).
31. K. Ogata, M. Toratani, and H. Murakami, "GCOM-C/SGLI Level-2 ocean color products generation," in *IGARSS 2017 - 2017 IEEE International Geoscience and Remote Sensing Symposium*, (2017), 5648–5649.
32. H. M. Dierssen, M. Gierach, L. S. Guild, *et al.*, "Synergies Between NASA's Hyperspectral Aquatic Missions PACE, GLIMR, and SBG: Opportunities for New Science and Applications," JGR Biogeosciences **128**(10), e2023JG007574 (2023).
33. G. Zibordi, F. Mélin, J.-F. Berthon, *et al.*, "AERONET-OC: a network for the validation of ocean color primary products," Journal of Atmospheric and Oceanic Technology **26**(8), 1634–1651 (2009).
34. F. Mélin and G. Sclep, "Band shifting for ocean color multi-spectral reflectance data," Opt. Express **23**(3), 2262–2279 (2015).
35. M. Talone, G. Zibordi, and J. Pitarch, "On the Application of AERONET-OC Multispectral Data to Assess Satellite-Derived Hyperspectral Rrs," IEEE Geosci. Remote Sensing Lett. **21**, 1–5 (2024).
36. S. W. Bailey and P. J. Werdell, "A multi-sensor approach for the on-orbit validation of ocean color satellite data products," Remote sensing of Environment **102**(1-2), 12–23 (2006).
37. Z. Lee, T. Wang, L. Zhao, *et al.*, "Cross-satellite atmospheric correction for consistent remote sensing reflectance from multiple ocean color satellites: Concept and demonstrations," J. Remote Sens. **4**, 0302 (2024).
38. M. Toratani, K. Ogata, K. Suzuki, *et al.*, "Gcom-C/Sgli Ocean Standard Products and Early Validation Results," in *IGARSS 2019 - 2019 IEEE International Geoscience and Remote Sensing Symposium*, (2019), 4741–4744.
39. S. I. Salem, M. Toratani, H. Higa, *et al.*, "Long-Term Evaluation of GCOM-C/SGLI Reflectance and Water Quality Products: Variability Among JAXA G-Portal and JASMES," Remote Sensing **17**(2), 221 (2025).
40. H. Murakami, D. Antoine, V. Vellucci, *et al.*, "System vicarious calibration of GCOM-C/SGLI visible and near-infrared channels," J. Oceanogr. **78**(4), 245–261 (2022).
41. M. Zhang, A. Ibrahim, B. A. Franz, *et al.*, "Estimating pixel-level uncertainty in ocean color retrievals from MODIS," Opt. Express **30**(17), 31415–31438 (2022).
42. M. Zhang, A. Ibrahim, B. A. Franz, *et al.*, "Spectral correlation in MODIS water-leaving reflectance retrieval uncertainty," Opt. Express **32**(2), 2490–2506 (2024).
43. Z. Ahmad, B. A. Franz, C. R. McClain, *et al.*, "New aerosol models for the retrieval of aerosol optical thickness and normalized water-leaving radiances from the SeaWiFS and MODIS sensors over coastal regions and open oceans," Appl. Opt. **49**(29), 5545–5560 (2010).
44. A. Ibrahim, B. A. Franz, Z. Ahmad, *et al.*, "Multiband atmospheric correction algorithm for ocean color retrievals," Front. Earth Sci. **7**, 116 (2019).

Optics EXPRESS

45. B. N. Holben, D. Tanré, A. Smirnov, *et al.*, "An emerging ground-based aerosol climatology: Aerosol optical depth from AERONET," J. Geophys. Res. **106**(D11), 12067–12097 (2001).
46. H. Murakami, "ATBD of GCOM-C ocean color atmospheric correction," (2020).
47. H. R. Gordon and M. Wang, "Retrieval of water-leaving radiance and aerosol optical thickness over the oceans with SeaWiFS: a preliminary algorithm," Appl. Opt. **33**(3), 443–452 (1994).
48. IOCCG, "Atmospheric correction for remotely-sensed ocean-colour products," (IOCCG, Dartmouth, Canada, 2010).
49. M. Wang, "Remote sensing of the ocean contributions from ultraviolet to near-infrared using the shortwave infrared bands: simulations," Appl. Opt. **46**(9), 1535–1547 (2007).
50. M. Wang, "A refinement for the Rayleigh radiance computation with variation of the atmospheric pressure," International J. Remote Sens. **26**(24), 5651–5663 (2005).
51. Z. Lee, S. Shang, C. Hu, *et al.*, "Spectral interdependence of remote-sensing reflectance and its implications on the design of ocean color satellite sensors," Appl. Opt. **53**(15), 3301–3310 (2014).
52. A. Morel and L. Prieur, "Analysis of variations in ocean color 1," Limnology and Oceanography **22**(4), 709–722 (1977).
53. Z. Lee and J. Tang, "The two faces of "Case-1" water," J. Remote Sens. **2022**, 9767452 (2022).
54. Z. Lee and C. Hu, "Global distribution of Case-1 waters: An analysis from SeaWiFS measurements," Remote Sensing of Environment **101**(2), 270–276 (2006).
55. T. Moisan and B. Mitchell, "UV absorption by mycosporine-like amino acids in Phaeocystis antarctica Karsten induced by photosynthetically available radiation," Marine Biology **138**(1), 217–227 (2001).
56. R. Bai, X. He, Y. Bai, *et al.*, "Characteristics of water leaving reflectance at ultraviolet wavelengths: radiative transfer simulations," Opt. Express **28**(20), 29714–29729 (2020).
57. C. D. Mobley, D. Stramski, W. P. Bissett, *et al.*, "Optical modeling of ocean waters: Is the case 1-case 2 classification still useful?" Oceanography **17**(2), 60–67 (2004).
58. Y. Wang, Z. Lee, M. Ondrusek, *et al.*, "An evaluation of remote sensing algorithms for the estimation of diffuse attenuation coefficients in the ultraviolet bands," Opt. Express **30**(5), 6640–6655 (2022).